Supplementary Information

Interfacial charge transfer weakens hydrogen bonds between water molecules to accelerate solar water evaporation

Liru Wang[a,b], Jinguo Lin[c], Yuanyuan Li[a], Yanan Yang[a,b], Xiaoting Liu[a], Zhe Wang[a], Feng Liu*[,c], Xiaotong Sun[a], Tian Yang[a,b], Nan Chen*[,a,b], Liangti Qu[d]

[a] Key Laboratory of Photoelectronic/Electrophotonic Conversion Materials, Key Laboratory of Cluster Science, Ministry of Education of China, School of Chemistry and Chemical Engineering, Beijing Institute of Technology, Beijing 100081, P. R. China.

[b] Yangtze Delta Region Academy of Beijing Institute of Technology, Jiaxing, 314019, China.

[c] State Key Laboratory of Nonlinear Mechanics Institute of Mechanics, Chinese Academy of Sciences, Beijing 100083, P. R. China.

[d] Key Laboratory of Organic Optoelectronics & Molecular Engineering, Ministry of Education, Department of Chemistry, Tsinghua University, Beijing 100084, China.

Correspondence authors: Nan Chen; Feng Liu.
Email: Nan Chen, gabechain@bit.edu.cn; Feng Liu, liufeng@imech.ac.cn

1. Supplementary Notes

Note S1. The porosity（Φ）of foams

Porosity (Φ) is one of the characteristics of porous materials and is the percentage of the internal pore volume to the total volume of the foam. The porosity of different foams is calculated by the following equation,[1-5]

$$\Phi = \left(1 - \frac{\rho}{\rho_0}\right) \times 100\%$$

where ρ is the bulk density of foam, derived from the ratio of mass to volume of the foam. ρ_0 is the skeleton density of graphite which is known to be 2.25 g cm^{-3}.[4]

Note S2. FTIR spectrum of water

In the Fourier Transform Infrared Reflection (FTIR) spectrum, the -OH stretching vibration peaks of water molecules are at 3200 cm^{-1}~3650 cm^{-1}, of which 3650 cm^{-1}~3590 cm^{-1} is considered to be free -OH peak, 3500 cm^{-1}~3200 cm^{-1} is considered to be -OH that forms intermolecular hydrogen bonds, and 3570 cm^{-1}~3450 cm^{-1} is considered to be -OH that forms intramolecular hydrogen bonds. The FTIR spectra of rGO, rGOFpl-5, rGOFpl-3, rGOFpl-2, rGOFpl-1, which were irradiated under 1 sun, their -OH stretching vibration peaks were located at 3288 cm^{-1}, 3234 cm^{-1}, 3227 cm^{-1}, 3261 cm^{-1}, 3273 cm^{-1}, respectively, compared with rGO, all -OH peaks of several rGOFpl were redshifted, this is because adjacent water molecules form stronger hydrogen bonds with the polar surface of Fpl nanosheets.

Note S3. The existing state of water

Water in the photothermal material exists in three states: free water (FW),

intermediate water (IW) and bound water (BW).[6-9] FW indicates that the water molecules are in an independent state and do not interact with other molecules; IW indicates that the water molecules are in a weak interaction state with the surface of the photothermal material, and BW indicates a strong interaction between the water molecules and the surface of the photothermal material. The interactions mentioned here usually refer to hydrogen bonds of different strengths. Water molecules tend to form hydrogen bonds with polar functional groups that are stronger than the hydrogen bonds between water molecules, thus forming BW. Once the hydrogen bonds formed between the BW molecules and the photothermal material are broken, they will interact with less than 4 water molecules to form IW. IW exhibit poor stability and only a small amount of energy is required for them to escape from the evaporation interface.[10-13] BW has no peak in the Raman spectrum because strong hydrogen bonds do not allow them to exhibit stretching vibrations. Except BW, the peak of FW is around 3200 cm^{-1}~3450 cm^{-1} and the peak of IW is around 3500 cm^{-1}~3650 cm^{-1}.[14-16] We measured the Raman spectra of the rGOFpl-5 and rGOFpl-3 samples infiltrated with water, and the subsequent Gaussian function fitting yielded four peaks (Tab. S5), In addition, rGO has a weak affinity for water and its water peak was not observed (Fig. S7). rGOFp1-5 had four peaks of 3264 cm^{-1}, 3437 cm^{-1}, 3546 cm^{-1}, 3640 cm^{-1}. The IW/FW ratio of 0.37 was obtained by integrating the peak areas. rGOFpl-3 had four peaks of 3276 cm^{-1}, 3434 cm^{-1}, 3533 cm^{-1}, 3637 cm^{-1}, and the IW/FW ratio of 0.4 was obtained by integrating the peak areas. We also measured the Raman spectrum of pure water and obtained a ratio of IW/FW of 0.23 (Fig. S8).

Note S4. Water evaporation performance of rGOFpl solar absorber

The prepared rGOFpl foams all have high porosity (>99%) and the porosity of the foams decreases slightly with the addition of Fpl. Microstructure optimization showed that despite the highest porosity of rGO, the van der Waals forces between the graphene sheets were weak and easy to stack. The vertical channels in GO are poorly formed after freeze-drying, leading to insufficient water supply during the photothermal process, as shown in Fig. S19. The water transport capacity in rGOFpl foams is improved and Fpl induces charge transfer with adjacent water molecules, resulting in weaker polarity of adjacent BW, which weakens the hydrogen bonds with IW molecules and makes IW molecules more prone to evaporation. Further addition of Fpl nanosheets with strong polar effect makes the 3D structure in GOFpl more complex and does not form obvious longitudinal channels, thus not conducive to water transport, as shown in Fig. S18.

Note S5. Computation details

First principle calculation. The polarity of matters is obtained by structure relaxations and self-consistently calculations by using the the projected augmented wave potentials [17] and the exchange-correlation functional is treated on the basis of the Perdew-Burke-Ernzerhof generalized gradient approximation, [18] implemented in the Vienna Ab initio Simulation Package (VASP). [19] For the Bernal-Fowler ice model, 350 eV is chosen for energy cutoff, “3×3×3” Monkhorst-Pack meshes is used and the electronic self-consistent step convergence is set to be 10^{-5} eV. While for the calculation of correlation between polarity and electronegativity difference, 400 eV is

chosen for energy cutoff and "6×6×1" and "1×1×1" Monkhorst-Pack meshes is used, respectively. The structural structures relaxations are done with the residual Hellman-Feynman force <10^{-3} eV/Å and electronic self-consistent step convergence is 10^{-5} eV. Based on the obtained charge distribution, the Bader charge analysis [20] is performed to evaluate the polarity.

Molecular dynamics (MD) simulation. In our study, the simple point charge (SPC) [21] model was used to simulate the evaporation dynamic process, where the total energy is given as

$$\phi_{\mathrm{tot}} = \phi_{\mathrm{coul}} + \phi_{\mathrm{vdw}}, \quad (1)$$

where the first term is the Coulomb interaction given by $\phi_{\mathrm{coul}} = \sum_i \sum_j (k_C\, q_i q_j / r_{ij})$, where k_C is the electrostatic constant, q_i and q_j are the partial charges relative to the charge of the electron, r_{ij} denotes the distance between two atoms or points charge. In original SPC potential, the partial charges equal 0.41 and -0.82 for H and O atoms, which is slightly changed here to study the polarity influence to evaporation rate. Besides, the van der Waals interaction between O atoms is described *via* Lennard-Jones potential, *i.e.* $\phi_{\mathrm{vdw}} = 4\varepsilon[(\sigma/r)^{12}-(\sigma/r)^{6}]$, where ε=0.00673 eV and σ=3.166 Å. Note that the rigid SPC model is considered here (*etc*. non-bonded and non-angled interactions within a water molecule), the equilibrium O-H distance and H-O-H angles are taken 1.0 Å and 109.47°.

The MD simulations were performed using the LAMMPS.[22] The initial configurations are generated randomly. Each periodic simulation box contains 500 water molecules and the relaxation at 300 K is employed 100000-time steps (time step

is set to 2 fs), where NVT ensemble is used for all the simulations.

2. Supplementary Figures

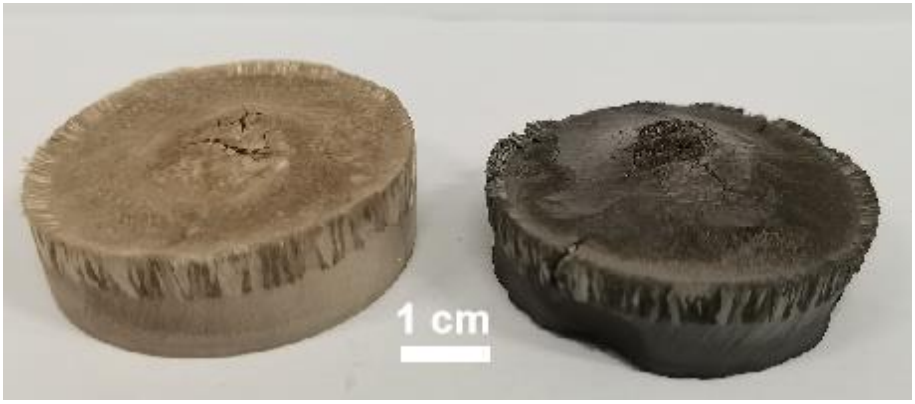

Fig. S1. Cylindrical samples before and after hydrazine vapor reduction (GOFpl on the left and rGOFpl on the right), d = 4.4 cm.

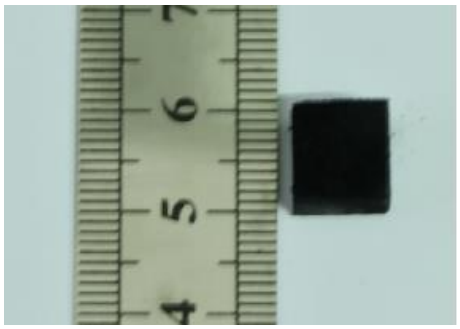

Fig. S2. The rGOFpl foam with an area of 1×1cm was obtained by laser cutting.

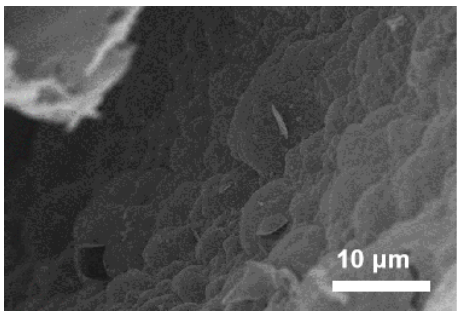

Fig. S3. SEM image of the surface of the rGOFpl foam show that graphene sheets form mountainou-like folds.

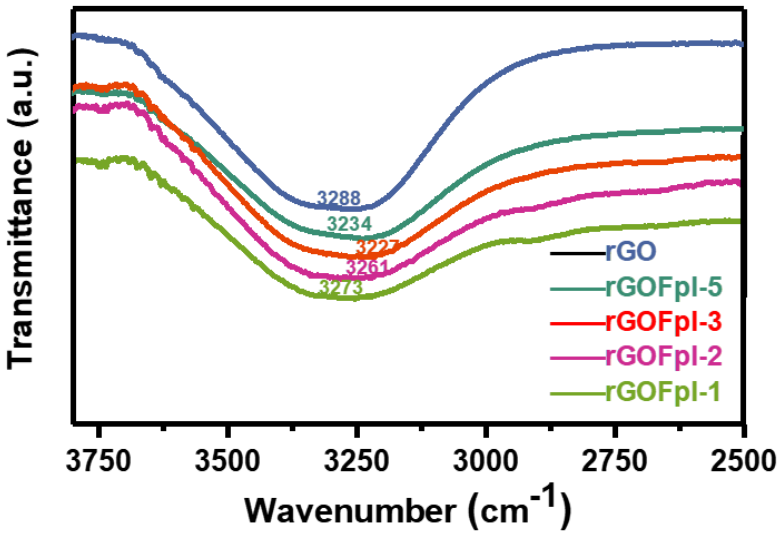

Fig. S4. Magnified view of the -OH peak redshift of water molecules in different rGOFpl foams.

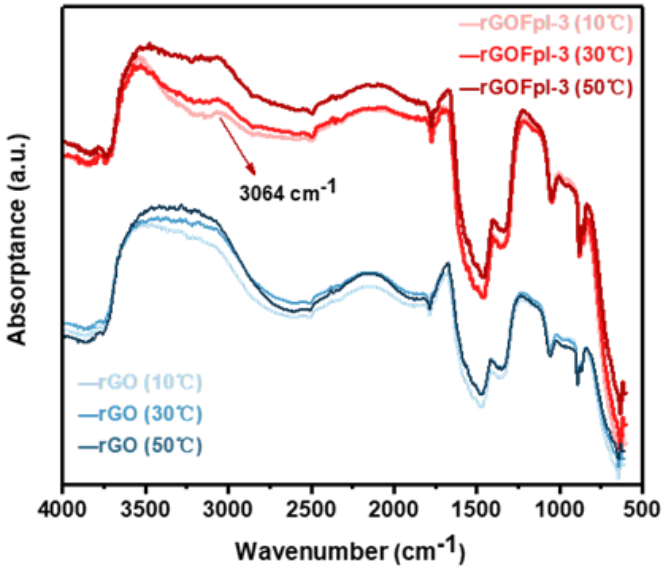

Fig. S5. *In-situ* DRIFT spectra at different temperatures of rGO and rGOFpl-3 foams.

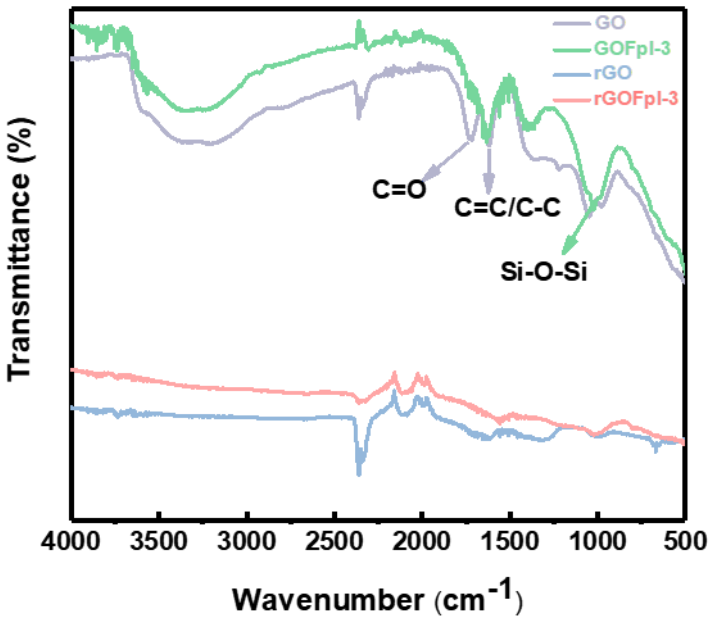

Fig. S6. FTIR spectra of dried GO, GOFpl-3, rGO, rGOFpl-3 foams.

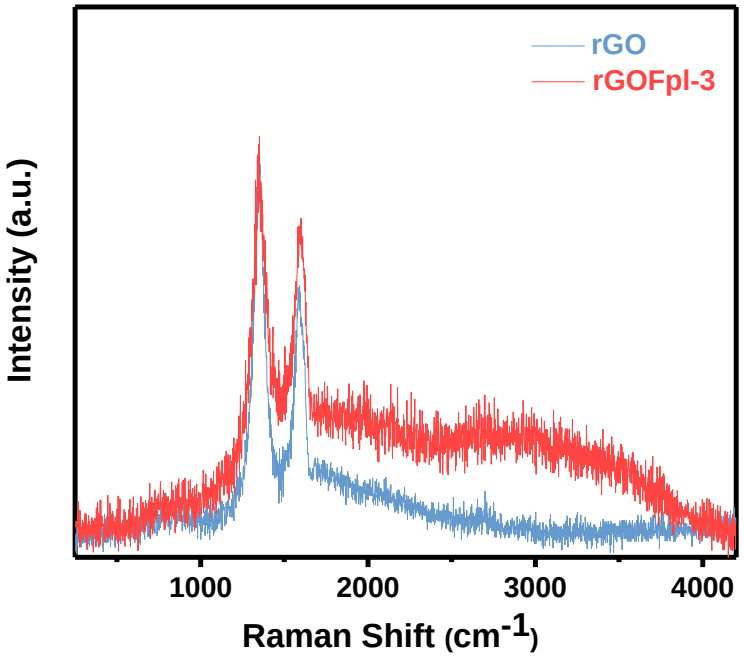

Fig. S7. Raman spectra of rGO and rGOFpl-3 foams in the moist state. rGOFpl-3 foam has more pronounced absorption peaks of water.

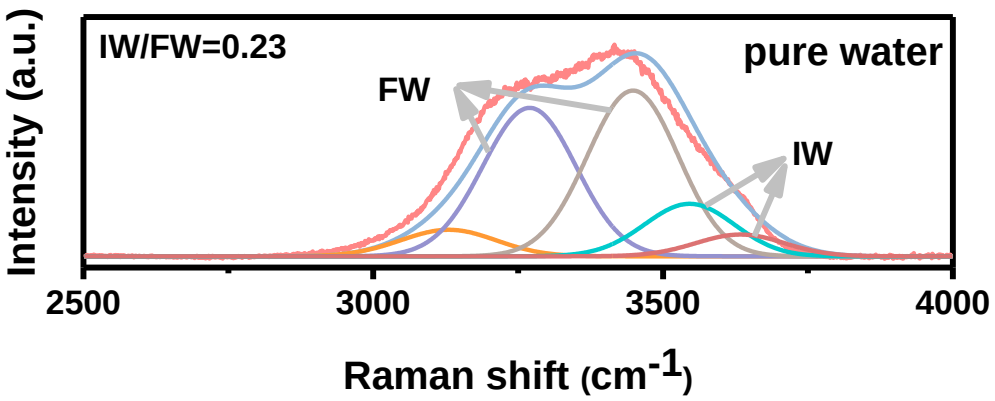

Fig. S8. Raman spectra with fitting curves showing FW and IW ratio in the pure water.

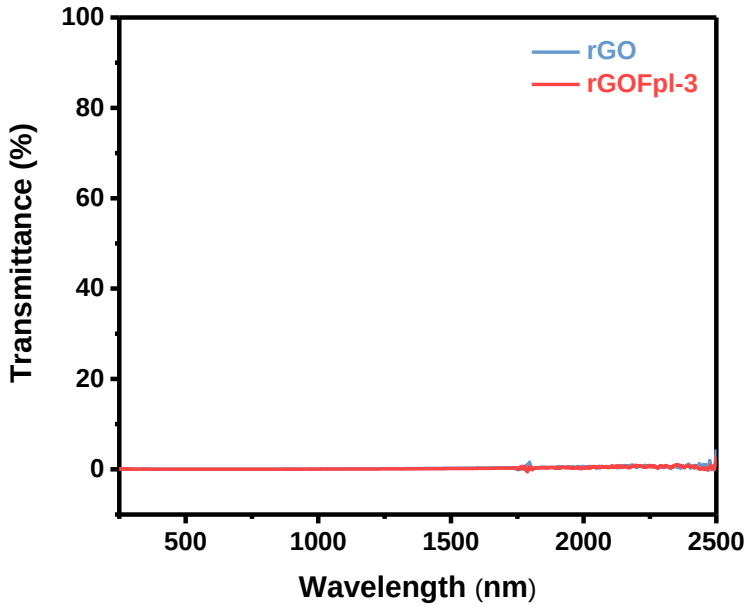

Fig. S9. Transmittance spectra of the rGO and rGOFpl-3 foams in the wavelength range of 200-2500 nm.

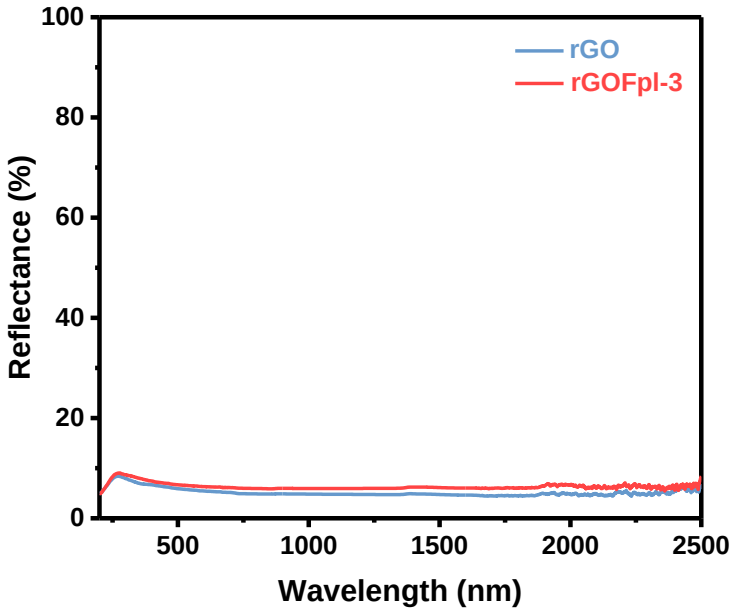

Fig. S10 Reflectance spectra of the rGO and rGOFpl-3 foams in the wavelength range of 200-2500 nm.

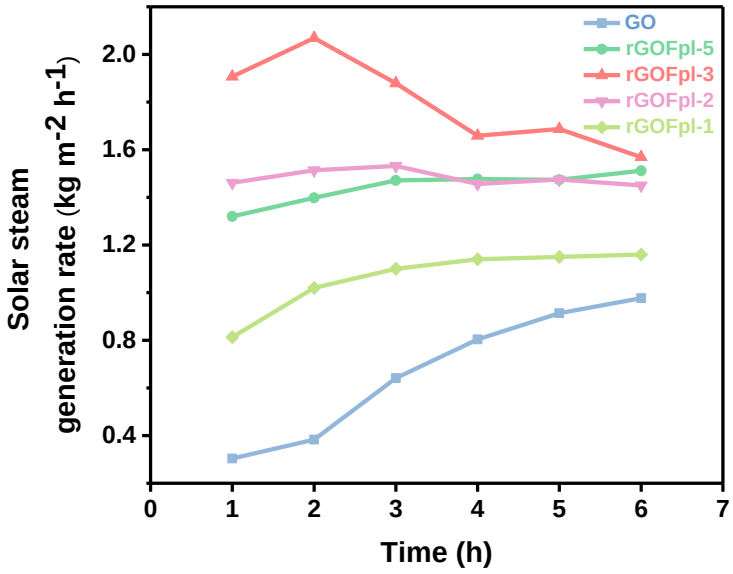

Fig. S11. Solar steam generation rate of rGO, rGOFpl-5, rGOFpl-3, rGOFpl-2, rGOFpl-1 foam within 6 h under 1 sun.

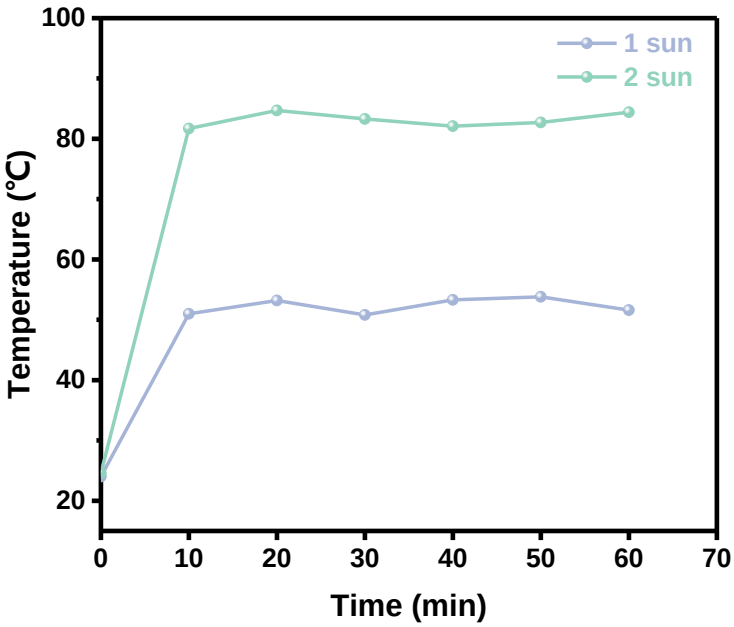

Fig. S12. The surface temperature change of the dried rGOFpl-3 foam under 1 sun and 2 sun irradiations within 60 min.

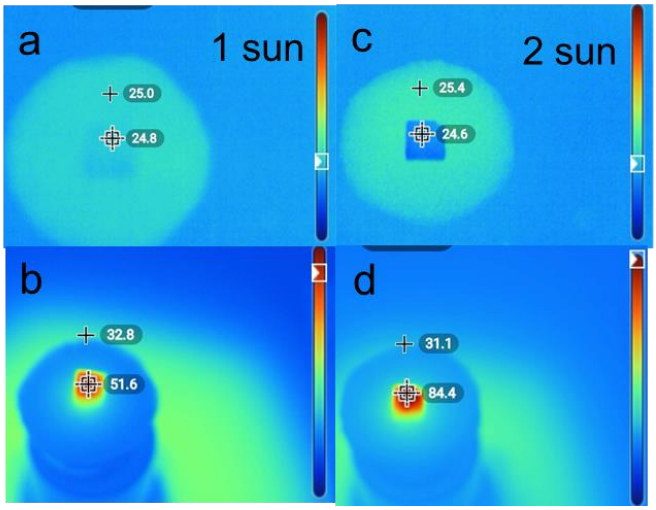

Fig. S13. Infrared thermographic images of the dried rGOFpl-3 foam under different sun irradiations. The photos of dried rGOFpl-3 foam a) before and b) after 1 sun irradiation. The photos of dried rGOFpl-3 foam c) before and d) after 2 sun irradiations.

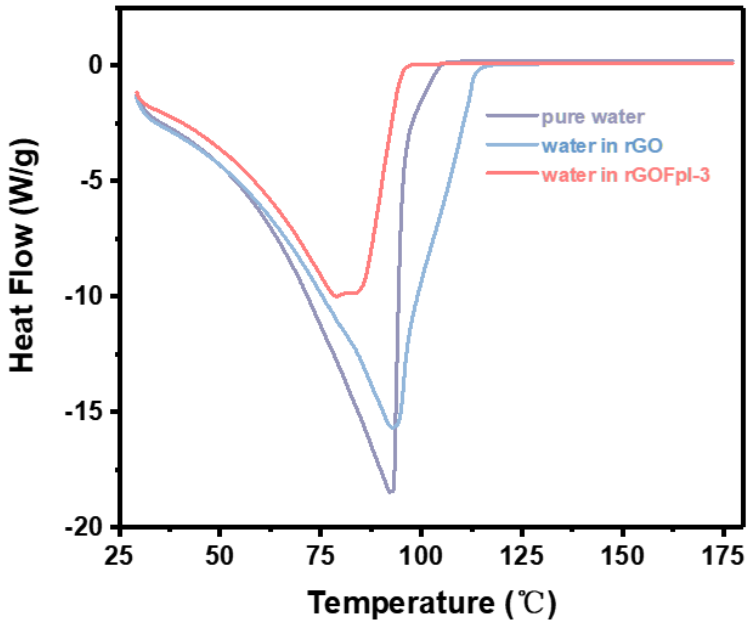

Fig. S14. DSC curves of rGO, rGOFpl-3 foam and pure water.

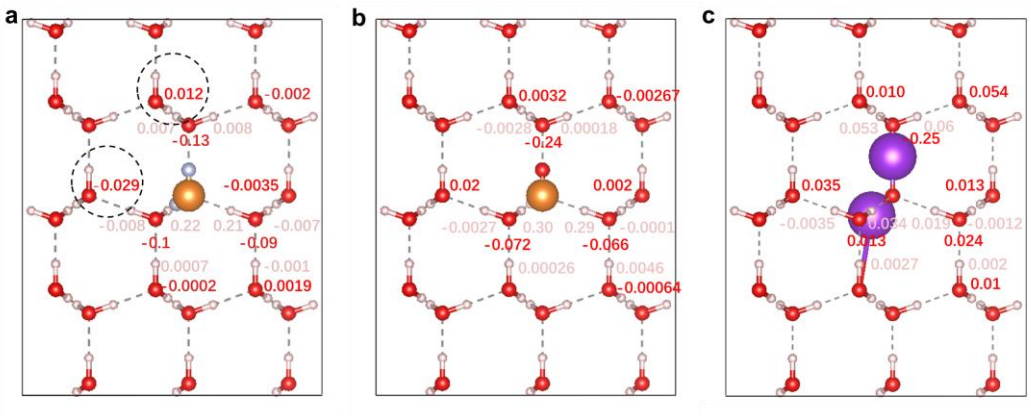

Fig. S15. Polarity model. The Bernal-Fowler ice model with three studied matters embedded is applied, where MgF_2, MgO and K_2O are shown in (a), (b) and (c), respectively. The red, pink, yellow, and purple color represent O, H, Mg, and K atoms, respectively. The corresponding gain (loss) of electrons is expressed by positive (negative) numbers. Note that O atoms obtain electrons, H atoms lose electrons suggesting weaker polarity of surrounded water molecule.

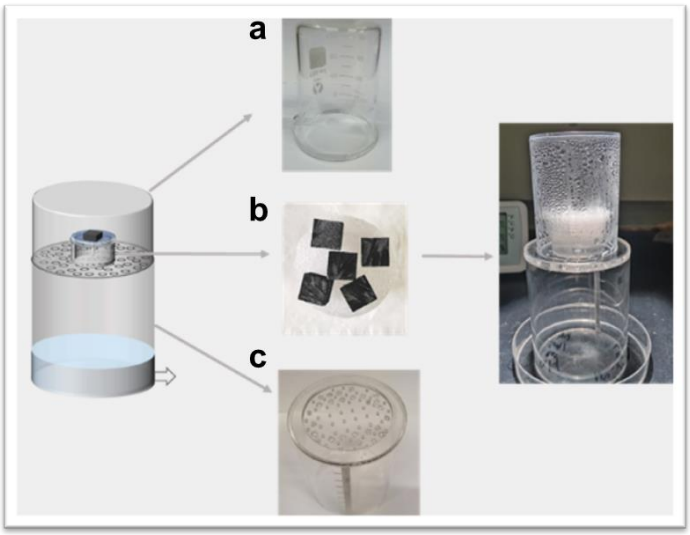

Fig. S16. Schematic diagram and physical diagram of water collection. It is mainly composed of three parts, part a) is a glass lid 10 cm high, where steam condenses on the walls of the lid to form droplets flowing downwards; Part b) is an evaporation device with the cotton stick passes through the middle of the thermal insulation layer (polystyrene foam) and supplies water to the sample from the water body for evaporation; Part c) is the water collection device with a certain number of small holes on the top. The condensated water flows down from the cover wall and flows into the collection device through the small holes.

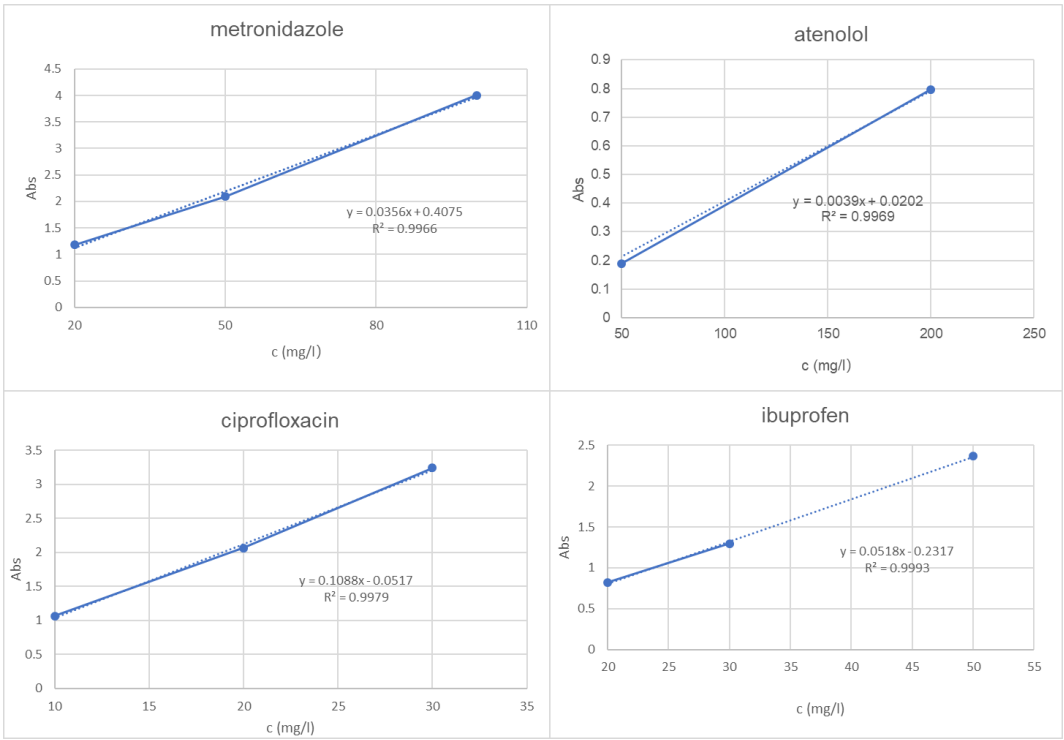

Fig. S17. Standard curves of UV-Vis absorption spectra of metronidazole, atenolol, ciprofloxacin, and ibuprofen drugs.

Fig. S18. SEM image of the cross section of rGOFpl-1 foam.

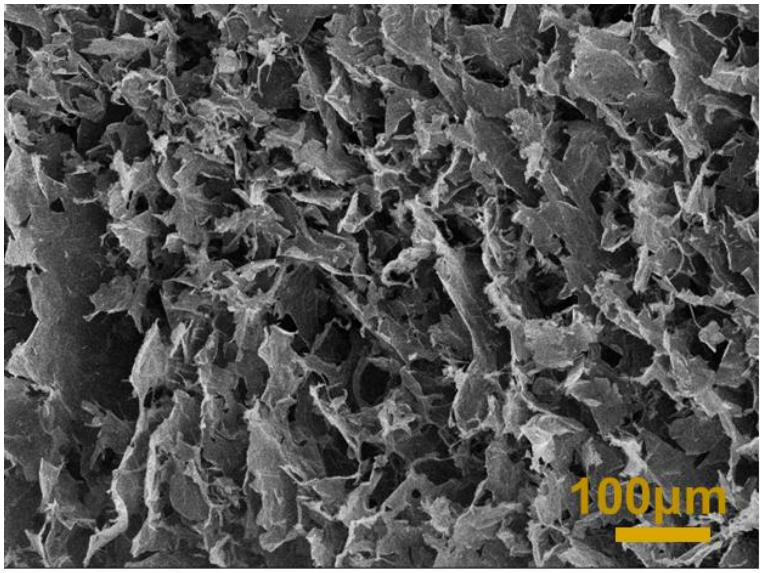

Fig. S19. The SEM image of the surface of rGO foam.

3. Supplementary Tables

Tab. S1. The bulk density (ρ) and the porosity（Φ）of foams

Type of foams	ρ (mg cm^{-3})	Φ (%)
rGO	6.17	99.7
rGOFpl-5	8.93	99.6
rGOFpl-3	10.00	99.6
rGOFpl-2	10.90	99.5
rGOFpl-1	19.30	99.1

Tab. S2. Elemental composition (%) of Fpl obtained by EDX analysis

Element	Weight %	Atomic %
O	37.50	49.30
F	11.50	12.73
Mg	15.39	13.31
Si	19.60	14.68
Al	5.66	4.41
K	10.34	5.56
Totals	**100.00**	

Tab. S3. Main elemental composition (%) of rGOFpl foam obtained by XPS analysis

Element	Atomic %
C	73.37
O	18.40
F	2.46
Si	2.11

Tab. S4. Main elemental composition (%) of rGOFpl foam obtained by EDX analysis

Element	Atomic %
C	76.77
O	16.22
F	2.61
Si	2.14

Tab. S5. Integral area of Gaussian function

	IW	BW	IW/FW
Pure water	254753	1110905	0.23
rGOFpl-5	835286	2229698	0.37
rGOFpl-3	2078050	2229698	0.40

Tab. S6. Comparison of water evaporation performance between rGOFpl and conventional rGO-based solar absorbers

Sample	Solar intensity	Evaporation rate (kg m^{-2} h^{-1})	Efficiency	Refs.
CB/rGO/PS@PSf	1 sun	1.11	73.0%	23
MXene@rGO	1 sun	1.33	85.2%	24
rGO/HNs	1 sun	1.48	89.2%	25
rGO-coated melamine	1 sun	1.43	89.6%	26
BC/CNT/rGO	1 sun	1.85	90.2%	27
CuS/rGO	1 sun	1.51	90.3%	28
KGM/rGO	1 sun	1.60	92.0%	29
rGO/Ag	1 sun	1.56	97.9%	30
in situ self-reduction of graphene oxide by geopolymer (rGOPGC)	1 sun	1.75	98.5%	31
rGOFpl foam	**1 sun**	**1.83**	**81.4%**	

References

1 L. L. Beranek, *J Acoust Soc Am* 1942, **13**, 248.
2 R. W. Leonard, *J Acoust Soc Am* 1948, **20**, 39.
3 Y. Champoux, M. R. Stinson, G. A. Daigle, *J Acoust Soc Am* 1991, **89**, 910.
4 S. Biloe, S. Mauran, *Carbon*, 2003, **41**, 525.
5 Z. L. Li, H. S. Yang, S. Lupi, *Adv. Mater. Interfaces* 2021, **8**, 2100227.
6 T. Hatakeyema, A. Yamauchi, H. Hatakeyema, *Eur. Polym. J.* 1984, **20**, 61.
7 T. Terada, Y. Maeda, H. Kitano, *J. Phys. Chem*. 1993, **97,** 3619.
8 Z. H. Ping, Q. T. Nguyen, S. M. Chen, *Polymer* 2001, **42**, 8461.
9 T. Wang, S. Gunasekaran, *J.Appl. Polym. Sci.* 2006, **101**, 3227.
10 K. Kudo, J. Ishida, G. Syuu, *J. Chem. Phys*. 2014, **140**, 044909.
11 Y. Sekine, T. Ikeda-Fukazawa, *J. Chem. Phys.* 2009, **130**, 034501.
12 K. Hara, T. Masuike, A. Nakamura, *Jpn. J. Appl. Phys.* 1995, **34,** 5700.
13 K. Hara, T. Masuike, A. Nakamura, *Phys. B.* 1996, **219**, 526.
14 F. Zhao, X. Y. Zhou, Y. Shi, *Nat. Nanotechnol*. 2018, **13**, 489.
15 X. Y. Zhou, Y. H. Guo, F. Zhao, *Adv. Mater.* 2020, **3**2, 2007012.
16 C. X. Li, S. J. Cao, J. Lutzki, *J. Am. Chem. Soc*. 2022, **144**, 3083.
17 P. E. Blöchl, *Phys. Rev. B* 1994, **50**, 17953.
18 J. P. Perdew, K. Burke, M. Ernzerhof, *Phys. Rev. Lett*. 1996, **77**, 3865.
19 G. Kresse, J. Furthmüller, *Phys. Rev. B* 1996, **54**, 11169.
20 H. J. C. Berendsen, J. P. M. Postma, W. F. van Gunsteren, *In Intermolecular forces; Springer,* Dordrecht, 1981, **pp331**.
21 G. Henkelman, A. Arnaldsson, H. Jónsson, *Comput. Mater. Sci*. 2006, **36** 254.
22 S. Plimpton, *Comput. Phys* 1995, **117**, 1.
23 H. Q. Fan, A. L. Gao, G. F. Zhang, *Chem. Eng. J*. 2021, **415**, 128798.
24 P. J. Ying, B. Ai, W. Hu, *Nano Energy* 2021, **89**, 106443.
25 Z. C. Xiong, Y. J. Zhu, D. D. Qin, *ACS Appl. Mater. Interfaces.* 2020, **12**, 32556.
26 C. Chang, M. Liu, L. Li, *J. Mater. Res.* 2022, **37,** 294.
27 M. T. Jin, Z. T. Wu, F. Y. Guan, *ACS Appl. Mater. Interfaces* 2022, **14**, 10, 12284.
28 F. T. Meng, Y. Zhang, S. F. Zhang, *Ind. Eng. Chem. Res*. 2022, **61**, 9763.
29 K. F. Yu, P. F. Shao, P. W. Meng, *J. Hazard. Mater.* 2020, **392**, 122350.
30 J. K. Xiao, J. Z. Gong, M. Dai, *J. Alloys Compd.*, 2023, **930**, 167404.
31 X. F. Deng, Y. Y. Ge, Y. He, *J. Hazard. Mater*. 2022, **424**, 127433.